# Magnetoresistance behavior of nanoscale antidot arrays

C. C. Wang and A. O. Adeyeye*
*Information Storage Materials Laboratory, Department of Electrical and Computer Engineering, National University of Singapore, 4 Engineering Drive 3, 117576 Singapore*

N. Singh
*Institute of Microelectronics, 11 Science Park Road, Singapore Science Park II, 117685 Singapore*

Y. S. Huang and Y. H. Wu
*Information Storage Materials Laboratory, Department of Electrical and Computer Engineering, National University of Singapore, 4 Engineering Drive 3, 117576 Singapore*

(Received 2 July 2005; revised manuscript received 14 September 2005; published 28 November 2005)

We investigate the transport properties of nanometer-scale $Ni_{80}Fe_{20}$ antidot arrays fabricated using deep ultraviolet lithography. Magnetotransport measurements have been shown as a powerful and sensitive technique in mapping the magnetization reversal process in complex magnetic structures. Compared with continuous film, a drastic increase in coercivity in the antidot structures due to local modification of the spin configurations was observed. We found that the current density distribution is periodically modulated by the presence of holes, which gives rise to the interesting high-field sloping behavior of the magnetoresistance (MR). The effect of antidot film thickness for fixed lateral geometry on the MR response was also investigated, and the reversal process was found to be strongly dependent on the antidot film thickness. Our experimental results were further verified by magnetic hysteresis measurements and micromagnetic simulations, which show good agreement with the experimental MR data.

DOI: 10.1103/PhysRevB.72.174426 PACS number(s): 75.47.−m, 75.60.Jk

## INTRODUCTION

The existence of imperfections such as grain boundaries, precipitates, inclusions, and other defects is responsible for the hysteresis phenomenon in ferromagnetic materials when the magnetization reversal mechanism is domain-wall movement.[1] These defects, which modulate the domain-wall energy locally, function as domain-wall pinning sites. Their size, magnetic parameters, and distribution can directly affect the magnetic properties of the material.[1–6] With the advances in nanofabrication and other controlled fabrication techniques, it is possible to create well-defined defects using lithographic techniques.[7–20] One typical structure that is formed by lateral arrays of holes in the contiguous film is commonly referred to as antidot structure.

Fundamentally, how the introduction of these nonmagnetic inclusions affects the magnetic behavior of the continuous film is of great interest and has received a lot of attention. One common finding from this structure is the magnetic "hardening" effect. As compared with continuous film, the antidot arrays have a dramatically enhanced coercivity, the magnitude of which is dependent on their size and distribution.[8,10,18] For instance, in the study of the permalloy film embedded with square holes, it was found that the coercive force is increased as the antidot size is reduced with a fixed size-to-separation ratio.[8] The presence of the holes can also induce well-defined magnetic domain patterns around them. The detailed domain structures observed at remanence are not only a function of the shape and packing fraction of antidots,[11,17] but also the lattice geometry.[13]

In experiment, the study of the magnetization reversal process of antidot structures has been mainly documented on antidot arrays at micron or submicron range using magneto-optic Kerr effect measurements,[10,12,13,16] magnetic force microscopy,[21] and Lorentz microscopy.[11,22] Magnetoresistance (MR) measurement technique, whose output depends on the direction of current density and local spins, is an alternative approach for probing the magnetic properties in these systems. MR measurements are clearly extensible to the nanoscale regime, and perhaps become easier for the smaller structures since the resistance values become larger and easier to measure. Although some other groups have attempted MR measurements on nanoscale antidot structure,[9,15,19] only limited information regarding the magnetization reversal process was obtained and discussed.

In this paper, we have fabricated large-area nanoscale square lattice antidot arrays using KrF deep ultraviolet (DUV) lithography. The antidot pitch is kept at 450 nm, and the diameter of the antidot is 300 nm. We performed a systematic study on the transport properties of the structure as a function of magnetic-field orientation and film thickness. We found that the current density distribution in the structures is not uniform. The detailed features signifying the switching process are clearly identified from the shape of the MR curves. We also observed a dramatic increase in coercivity of the antidot arrays compared with the continuous film with the same thickness due to the local modification of spin rotation. From our film-thickness-dependent study, we found that the coercive field and the reversal behavior of the antidot arrays could be engineered by changing the film thickness. We have correlated our magnetoresistance curves with the magnetic hysteresis loops measured using the vibrating sample magnetometer (VSM). The magnetization reversal process in the antidot arrays was further supported by a

 

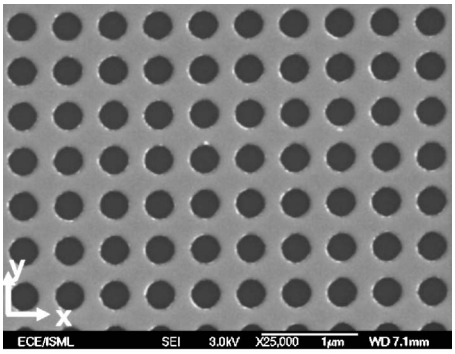


(a)

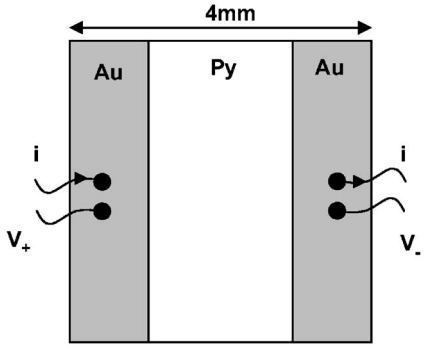


(b)

FIG. 1. (a) Scanning electron micrograph of $Ni_{80}Fe_{20}$ antidot arrays. (b) Electrical contact geometry used for MR measurements.

simple micromagnetic simulation, and the modeling on the MR curves shows good agreement with the experimental results.

## EXPERIMENTAL DETAILS

In our experiments, large-area $Ni_{80}Fe_{20}$ antidot structures ($4\times4$ mm$^2$) were fabricated on commercially available silicon substrate using optical lithography at 248 nm exposing wavelength. To create patterns in resist, the substrate was coated with a 60-nm-thick anti-reflective layer followed by a 480 nm positive DUV photoresist, which is four to five times thicker than those used in electron beam lithography. This allows for the fabrication of antidots with high aspect ratio and makes the lift-off process easier. A Nikon lithographic scanner with KrF excimer laser radiation was used in exposing the resist. The antidot pitch on the mask was kept at 450 nm. To convert the resist patterns into antidots, ferromagnetic material $Ni_{80}Fe_{20}$ was deposited using e-beam evaporation technique. The pressure was maintained at $2\times10^{-6}$ Torr during deposition. Lift-off of the deposited film was carried out in isopropyl alcohol (IPA). Completion of the lift-off process was determined by the color contrast of the patterned $Ni_{80}Fe_{20}$ area. The final structure consists of $Ni_{80}Fe_{20}$ antidot arrays of diameter 300 nm and edge-to-edge spacing of 150 nm, as shown in Fig. 1(a). Details of the fabrication process are described in Ref. 23.

In order to probe the transport properties of the fabricated antidot array structures, electrical contacts were made on the pattern using standard optical lithography, metallization, and lift-off of Cr(100 Å)/Au(3000 Å), as illustrated in Fig. 1(b). The choice of the contact geometry is unconventional, as it is not the standard in-line four-point technique. The reason is that for large-area magnetic film, the conventional technique causes nonuniform current density distribution, and is less sensitive to the magnetoresistivity.[20,24] We observed in our previous work that the in-line four-point technique could completely change the sign of the magnetoresistance response in rectangular antidot structures, due to the presence of orthogonal current flow.[20] In order to circumvent this complication, the special contact geometry used will ensure uni-directional current flow in the perforated film. For MR measurements, a dc current of 1 mA was passed along the $x$ direction, and the resistance was recorded automatically as the in-plane magnetic field was swept. The devices were mounted on an automatic rotary stage that allows for the easy rotation of the devices in the magnetic field. Magnetic hysteresis loops were obtained using VSM at room temperature.

## RESULTS AND DISCUSSION

### Room-temperature MR

It is well known that the resistance of the ferromagnetic material can be described as

$$R_{(H)} = R_{\perp} + \Delta R \cos^2 \theta, \tag{1}$$

where $\theta$ is the angle between the current density and magnetization, $R$ is the film resistance, and $\Delta R = R_{\parallel} - R_{\perp}$ represents the anisotropic MR (AMR) effect.

Since the AMR output depends on two physical terms, the current density and magnetization, it is important to first establish the current density distribution in our antidot structure in order to understand the varying magnetization component. Strictly speaking, the two terms are interdependent. However, due to the small change in AMR percentage ($\sim$2.5% for thin film), the correlation between the two could be ignored most of the time. Figure 2 shows the finite-element simulation for the current density distribution without taking into account the galvanomagnetic effect in the circular hole arrays. The arrows signify the direction of current flow at each location, and the length of the arrow indicates the magnitude of the current density. We observed that the current is unidirectional, with the major component pointing along the $x$ direction. We also noticed that the current density is not uniform but rather periodically modulated by the presence of the antidots. Nearer to geometrical boundary of antidots, the current tends to follow the circumferences of the holes. Deviation from the main current direction and a decrease in current density magnitude are observed as the current density penetrates into the region between the adjacent holes in the same row. Similar observation was also made in square antidot structure.[25,26]

Having established the current distribution in the structure, the MR response could be explained as a measure of the preference of the local spins along the current density direction. Shown in Fig. 3(a) is the normalized longitudinal MR

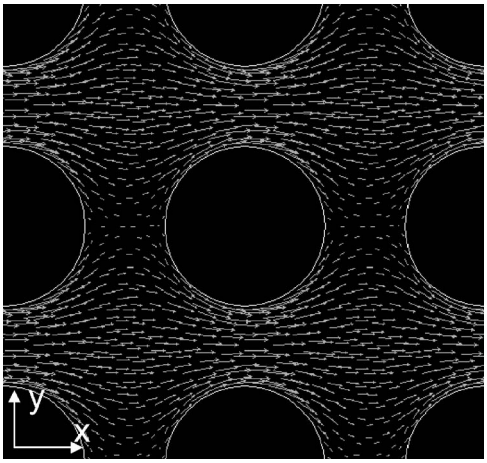


FIG. 2. Finite-element current density simulation for the circular antidot arrays. The length of the arrow indicates the magnitude of the current density.

(LMR) curve for 25-nm-thick $Ni_{80}Fe_{20}$ antidot arrays for fields applied along the probing current direction. The normalized percentage is defined as

$$\frac{\partial R}{R}\% = \frac{R_{(H)} - R_{(0)}}{R_{(0)}} \times 100, \tag{2}$$

where $R_{(H)}$ is the resistance of the device at a given applied field and $R_{(0)}$ is the resistance at zero field. The gray dots represent the loop with the field sweep from the negative saturation field to the positive field. The dark dots are the results for the reverse field sweep. We will only examine the loop marked by dark dots, as the two loops are essentially symmetric in nature. Shown as insets in Fig. 3(a) are the sketches of spin states of a unit cell at different field strength, inferred from the MR curve with simple magnetostatics and shape anisotropy. At first glance, the MR curve shows two distinct minima, with a series of bends signifying the switching process in the arrays.

At saturation field, all the spins in the antidot structure are aligned along the field direction, as shown in the schematic illustration *A* in Fig. 3(a). With the initial reduction of field, we observed a slight linear increase in resistance, indicating that the local spins are more aligned with the current density. This is because the current density is not exactly aligned with the magnetization at saturation, due to the geometrical confinement introduced by the holes, as shown in Fig. 2. At a slightly lower field, the spins close to the holes start to align along the edges of the holes to reduce the associated magnetostatic energy, as illustrated by spin state *B* in Fig. 3(a). Thus, the average angle between the current density and local spins is reduced, resulting in a higher resistance according to Eq. (1). As the field is reduced further, we observed a decrease in resistance followed by a kink at a field of 300 Oe as marked by position *a* in Fig. 3(a). This could be attributed to the continuous relaxation of the spins as shown in *B* starting to deviate from the local current density, which causes the initial decrease in resistance. Starting from position *a*, due to the high shape anisotropy the local spins to the left

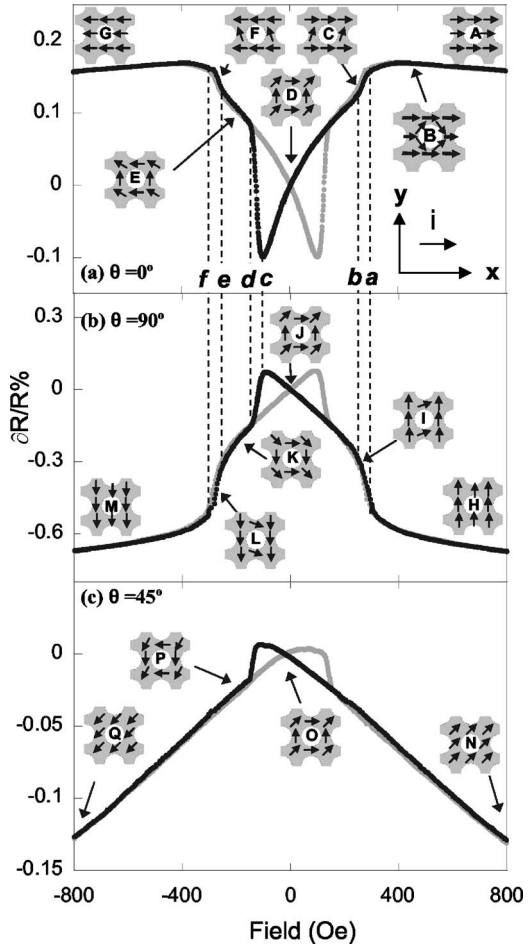


FIG. 3. Normalized MR curve for the 25 nm $Ni_{80}Fe_{20}$ antidot arrays as a function of field orientation. The gray dots represent the loop with field sweeping from the negative direction to the positive, and the dark dots are the results as the field sweeps back. Shown as insets are the schematic illustrations for the spin states at different field values. The dashed lines indicate the positions where discontinuities in the MR curve occur.

and right of the holes start to relax along the *y* direction, as illustrated by the inset *C*. This increase in the misalignment of the current density and magnetization at those areas could be responsible for the faster decrease in resistance. The decrease in resistance becomes gradual again at a field of 238 Oe, as shown at position *b*, indicating the completion of the previous spin rotation process. As the field is reduced to zero, the resistance is further reduced due to the spins at the corners to the holes rotating close to 45° to the *x* direction, causing a larger angle between the current density and magnetization, as shown in *D*. This configuration minimizes magnetostatic energy and avoids the net charges around the holes.

As the field changes sign, and increases in magnitude, the resistance decreases continuously. At this field range, due to the strong shape anisotropy imposed by the holes, the reverse domain could not be formed in the arrays initially, and the resistance decrease may still be attributed to the continual rotation of the diagonal spins. At a field of −105 Oe (position *c*), the irreversible switching to reverse magnetization state

occurs, as signified by the sudden jump in the curve. The field where the irreversible switching occurs also corresponds to the coercivity from the magnetization hysteresis loop.[8] The steep jump soon becomes gradual after position *d*, as the spins to the corner of the holes start getting pinned along the negative *x* axis, attaining a spin configuration shown in the spin state *E*. The completion of this process changes the deflection of the curve at a field of −220 Oe, as shown by position *e*. Further increase in reverse field magnitude causes the spins at the left and right side of the holes to rotate to the field direction as depicted in the spin state *F*, and the kink at position *f* shows that this process is over. A similar linear decrease with field is observed again, as the field approaches the reverse saturation field.

Figure 3(b) is the corresponding transverse MR (TMR) curve, where the in-plane field is applied perpendicular to the current ($\theta=90°$). The curve consists of a near-parabolic trace with extensive tails at high field and two distinctive peaks at low field. At saturation, the spins are perpendicular to the current, resulting in a low resistance, as shown in the spin state *H*. As the external field is reduced, at first the magnetization above and below the holes starts to relax along the current direction causing an overall increase in resistance, as shown in the spin state *I*. The relaxation of the spins diagonal to the holes, as shown in the spin state *J*, continues to increase the resistance value until at a reverse field, where irreversible switching in magnetization occurs and reaches spin state *K*. As the field increases in the reverse direction, the spins diagonal to the hole are pinned along the field, leading to a further decrease in resistance, as shown by state *L*. This decrease starts to become stable after the spins below and above the holes are perpendicular to the current in the opposite direction, as sketched in the spin state *M*. We can clearly see that the magnetization reversal process observed above is very similar to the one of LMR. Due to the symmetry of the square lattice, the TMR measurement could be also described as keeping the field direction as in LMR and then rotating the current direction by 90°. Hence, the two curves are actually describing the same magnetization reversal process, and this is evident from the spin state illustration and the switching positions marked by the dotted lines, as shown in Figs. 3(a) and 3(b).

For field applied at 45 degrees to the sense current, the MR curve is hard to saturate and is composed of a wide reversible field range, as shown in Fig. 3(c). The resistance increases almost linearly as the field is reduced from positive maximum. As depicted in the spin state *N* and *O* of Fig. 3(c), the increase in resistance is mainly due to the spins below and above the holes starting to align along the current density. A dip in resistance occurs at the negative field, where the spin state starts to become unstable, and has an abrupt switching to attain a new configuration shown in the spin state *P*. Further increase in field causes a linear decrease in resistance, as the spins start to rotate toward the field again in the reverse direction. We have thus shown that magnetotransport technique is a sensitive probe of the magnetization reversal process in complex antidot nanostructures.

As compared with the perforated film, the 25-nm-thick $Ni_{80}Fe_{20}$ continuous film deposited under the same condition shows completely different MR characteristics. The continuous film displays a typical positive magnetoresistance for LMR and negative magnetoresistance for TMR measurement with a low saturation field of about 10 Oe and coercivity at only 1.2 Oe. The MR behavior of the continuous film can be explained by the low intrinsic magnetic anisotropy of the $Ni_{80}Fe_{20}$ film and the weak hindrance for domain-wall propagation arising from the randomly distributed intrinsic imperfections in the film.

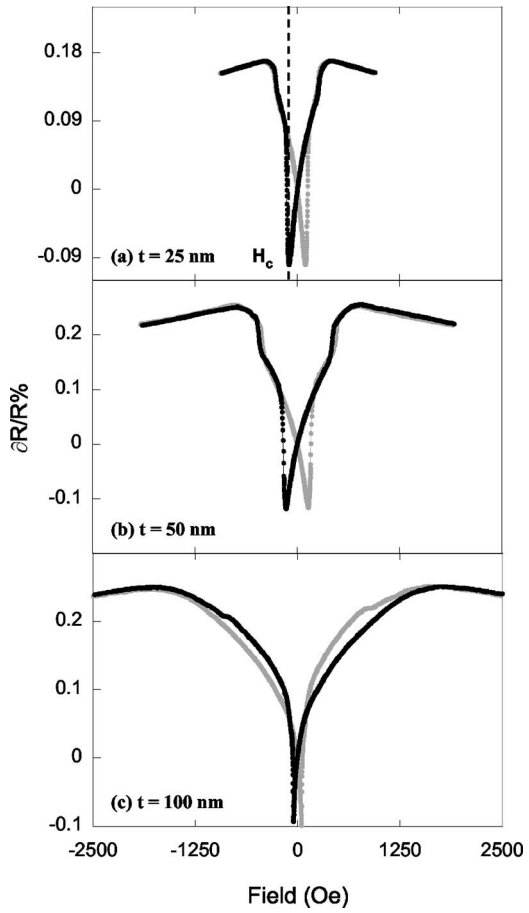


FIG. 4. Normalized LMR for antidot arrays with film thickness $t=25$, 50, and 100 nm, respectively.

### Thickness dependence of MR

To further understand the magnetoresistance behavior of the antidot array, we have conducted detailed thickness-dependent studies. In this experiment, the lattice geometry of the antidot arrays was fixed while the film thickness was varied. Figure 4 shows the LMR as a function of $Ni_{80}Fe_{20}$ film thickness ($t$). It can be seen that as $t$ increases to 50 nm, the shape of the MR curve is well preserved implying that the reversal process is similar to that described in Fig. 4 for the 25-nm-thick antidot arrays. The coercive field ($H_c$), however, has increased to 134 Oe, and saturation field has also increased. As $t$ is further increased to 100 nm, we observed a dramatic change in the MR response. As shown in Fig. 4(c), though the saturation field continues to increase, $H_c$ drops significantly to 50 Oe. A series of bends seen in the MR curves for $t \leqslant 50$ nm has been replaced by a gradual decrease

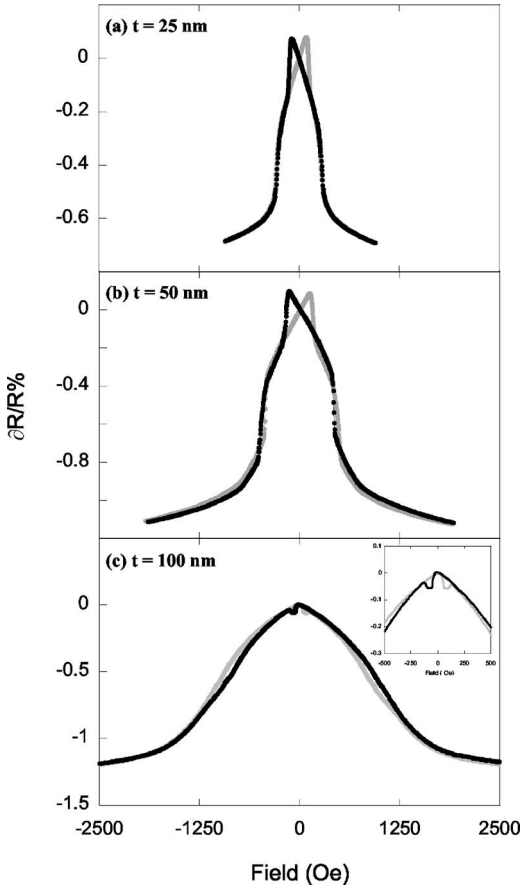


FIG. 5. Normalized TMR for antidot arrays with film thickness $t=25$, 50, and 100 nm, respectively.

and increase in resistance. The increase in saturation field with film thickness for the antidot arrays is a direct consequence of the increase of in-plane demagnetizing field. The initial increase in $H_c$ as $t$ increases could be attributed to the fact that 50-nm-thick antidot arrays are thermally more stable than 25-nm-thick antidot arrays, as similarly observed by other authors.[9] For $t=100$ nm, the film thickness is comparable to the dimension of the material between holes. In this regime, the magnetization ceases to be constrained rigidly to the plane of the film, and the reversal now involves a three-dimensional (3D) mechanism, which could probably contribute to the smooth change in magnetization and the drop in coercivity. Thus, the in-plane spin rotation mechanism used in explaining the reversal for $t \leqslant 50$ nm is no longer applicable here. Due to the complication of 3D reversal mechanism, we cannot exactly tell how the magnetization evolves, and the demanding computational power limits the use of micromagnetic simulation. However, a similar trend of thickness dependence of coercivity was observed in the study of nanowires. It was found that the dramatic decrease in coercivity with thickness is due to the change in reversal process.[27]

The corresponding TMR curves as a function of $Ni_{80}Fe_{20}$ thickness are shown in Fig. 5. Again, as film thickness increases to 50 nm, the shape of the MR curve is identical to that of 25-nm-thick antidot structures described in Fig. 3. For $t=100$ nm, however, the MR curve has markedly changed to a complete bell shape with a small valley after the field changes sign, as shown in Fig. 5(c). The valley occurs just after the coercive field shown in Fig. 4(c), and interestingly it does not have the corresponding transition in the LMR curve. Though the detailed spin state in the valley cannot be easily determined from the curve, it is clear that the system is trapped in a local energy minimum point within that field range. Due to the increase in in-plane demagnetizing field with film thickness, it is possible that this local minimum is created by the spins with a certain amount of out-of-plane components. The increase in resistance after the dip is thus a result from the external field forcing the out-of-plane spin components to be in the film plane. This reversal process can also make a positive contribution in the LMR measurement after irreversible switching, which occurs in conjunction with the resistance increase due to the in-plane spin rotation as illustrated in Fig. 3(a). This explanation in turn answers the question of the missing correspondence of the valley in the LMR curve.

### Magnetization hysteresis loops

Our ability to make large area samples by KrF lithography renders the characterization of antidot arrays using this conventional magnetometry possible. In this case, we have correlated our magnetoresistance results with $M$-$H$ loop measurements using VSM. Shown on the left panel of Fig. 6 are the normalized $(M/M_s)$ $M$-$H$ loops obtained for fields applied along the $x$ direction for $t=25$, 50, and 100 nm. It can be seen that features from the $M$-$H$ loop have their reminiscence in the corresponding LMR curves. For example, the coercivity which corresponds to the switching field in the MR curve and the saturation field follow the same trend as the LMR traces shown in Fig. 4. Similarly, the shape of the $M$-$H$ loop for $t=100$ nm has fewer kinks than the loops for $t=25$ and 50 nm during the magnetization reversal process.

However, the correlation between the $M$-$H$ loop and MR curves can be best seen by estimating LMR response from the hysteresis data. $M$-$H$ measurements provide a direct observation of average magnetization along the positive external field direction, i.e., the $x$ direction. If we assume that the current density distribution along the $x$ direction is uniform, the MR variation could be calculated as $(M/M_s)^2$ according to Eq. (1). It is evident from the calculation that the MR output is more sensitive to the magnetization change, since it collects the signal of the amplified magnetization. Shown on the right panel of Fig. 6 is the calculated MR from the hysteresis data. We can see that, for a field well below the nucleation field, the shape of the deduced MR curve bears a close resemblance to their corresponding experimental MR data depicted in Fig. 4, and all the magnetization switching events described before can be clearly identified from the curves. It should be noted that the calculation fails to reproduce the high-field sloping behavior observed in the LMR measurements, due to the negligence of detailed current density distribution. However, it is interesting to note that well beyond the nucleation field, the slope continues, as can be seen in Fig. 4. This is due to the suppression of spin scattering beyond saturation, as suggested in Ref. 15.

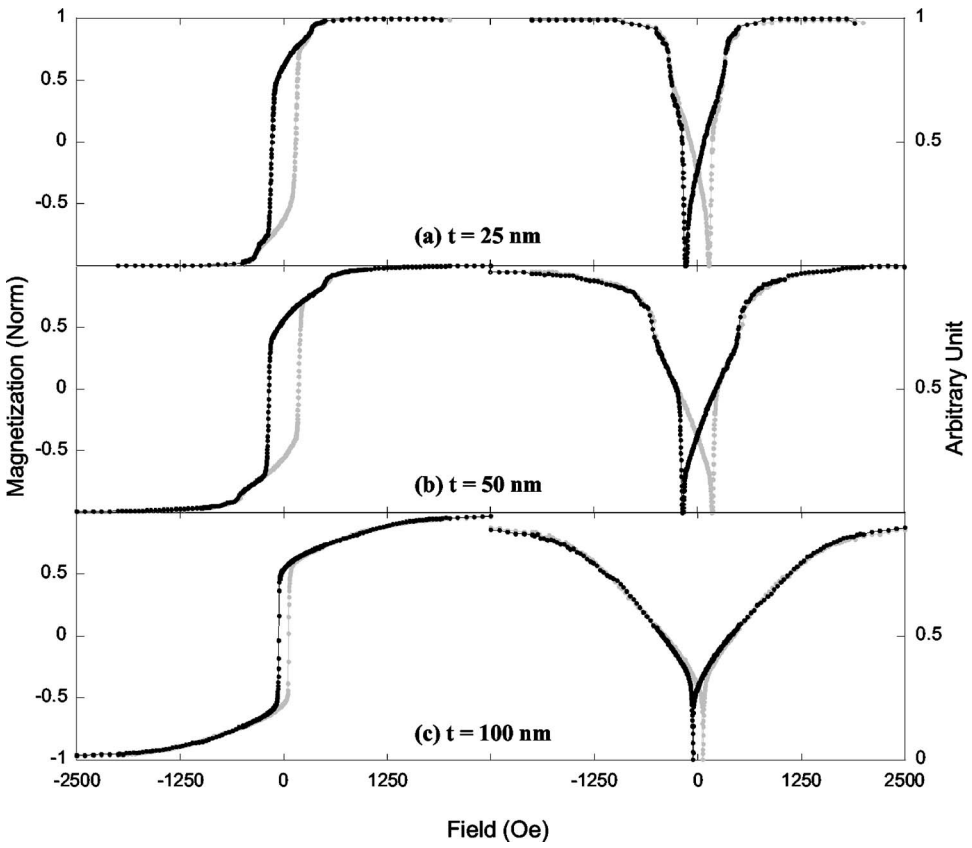


FIG. 6. Normalized *M-H* loops (left panel) and deduced LMR responses (right panel) as a function of the film thickness for field applied along the *x* direction.

### MR modeling

In order to correlate the experimental results with the theoretical prediction, micromagnetic simulations were performed using the Object Oriented Micromagnetic Framework (OOMMF) code from NIST.[28] This program integrates the Landau-Lifshitz equation on a 2D grid with 3D magnetization spins. The geometry of the model, which consists of 25 cell units, is shown in Fig. 7(a). The magnetic parameters used for simulation are saturation magnetization $M_s = 860$ kA/m, exchange constant $A = 13 \times 10^{-12}$ J m$^{-1}$, and anisotropy constant $K_u = 0$. Cell size is chosen to be 5 nm. The convergence criterion was a misalignment between magnetization and effective field ($|m \times h|$) lower than $10^{-5}$ in every computation cell. We simulated the magnetization state of the structure with the identical dimensions as shown in Fig. 1(a) for film thickness at 25 nm.

To reduce the boundary effect as pointed out by Guedes *et al.*[16] in our calculation, we extracted the reversal behavior of only the central unit from our simulation, as illustrated in gray in Fig. 7(a). For transport modeling, in order to take into account the inhomogeneous current distribution in Fig. 2, we used a simplified distribution of currents, being zero in between the holes along the current direction and finite but constant in the remaining region, as shown in Fig. 7(b). The AMR is calculated by averaging all the resistivity of each cell at a field value, using

$$\rho_{(H)} = \rho_0 + \frac{1}{V_c^2 n} \sum_i [k(\mathbf{m_i} \cdot \hat{\mathbf{j}})^2]. \tag{3}$$

Here, $\rho_0$, $n$, $V_c$, $\mathbf{m_i}$, $\mathbf{j}$, and $k$ are the normal resistivity, the number of cells, the volume of one cell, the moment of cell $i$, the unit vector of the current, and the AMR coefficient, respectively. We discard $\rho_0$ and normalize the constant coefficients in simulation as

$$X_{\mathrm{AMR}} = \frac{1}{n} \hat{\mathbf{j}} \cdot \sum_i [(\mathbf{m_i} \cdot \hat{\mathbf{j}}) \mathbf{m_i}]. \tag{4}$$

The simulated LMR and TMR results for antidot arrays with $t = 25$ nm are shown in Figs. 8(a) and 8(b), respectively. For clarity, we only show the trace when the field is swept from positive saturation to negative.

From the figures, we can see that the modeling has good agreement with the experimental curves. The simulated curves are characterized by prominent discontinuous jumps, which correspond to the major switching events in the structure. Most of these features can be easily associated with our experimental MR response in Fig. 3, and labeled accordingly in Fig. 8. The detailed spin states in Fig. 8(a) from OOMMF simulation further confirm the schematic spin illustrations in Fig. 3. However, the simulated MR curves are a lot more jagged than the actual experimental curve, and the sharp transitions in the modeling have become broadened in the real experiment, because the actual response is obtained from an average behavior of millions of cell units in the system. It was also observed that the coercive field of the simulated curve is at 200 Oe, which is much higher than from experiment, and it could be due to the thermal fluctuation effect which reduces the switching barrier for the samples and inaccuracy from the limited number of cell units for the simulation. We should also note that the simulation still assumes a uniform current density. Consequently, we observe a mono-

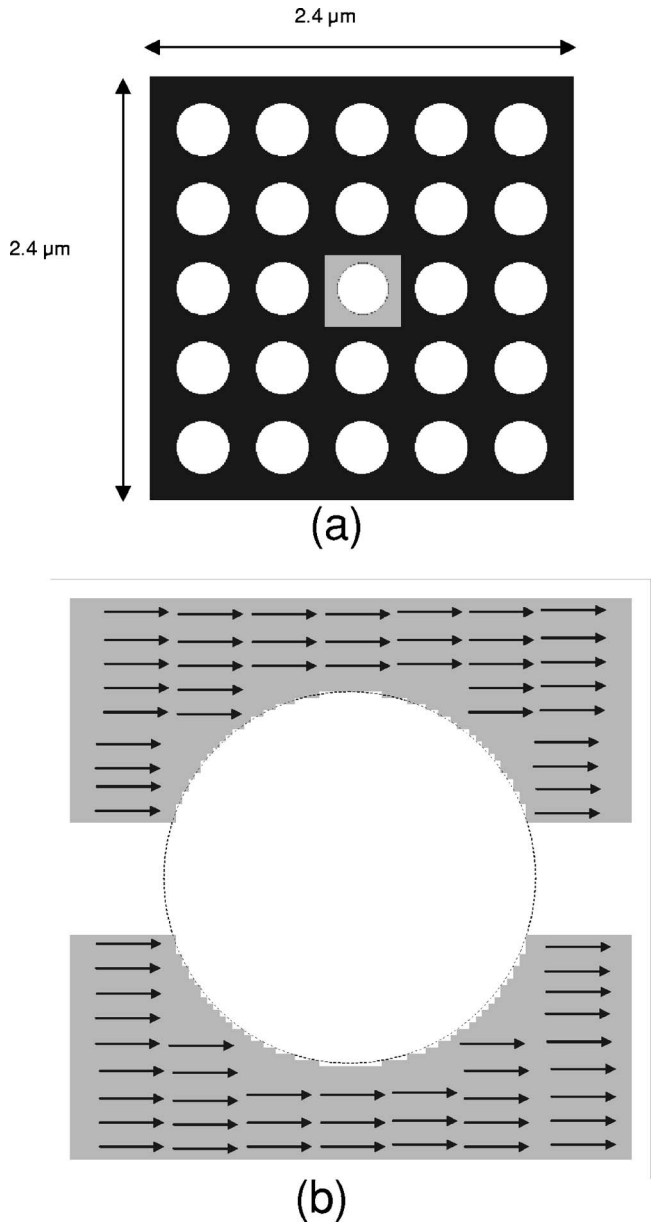


FIG. 7. (a) Schematic of the geometry of the model used in micromagnetic simulation. The shaded area is the central unit lattice selected for MR curve simulation. (b) The geometry extracted for the final MR modeling. A uniform current density distribution is assumed for the modeling, as illustrated by the arrows.

tonic decrease in resistance as the field is reduced from saturation field, which is very similar to the deduced MR curve from the *M-H* loop as shown in Fig. 6(a).

The good agreement between the experimental and simulation seems to reveal that the whole magnetization reversal process is dominated by spin rotation rather than domain-wall propagation. The apparent reason for this picture is that the explanation has been based on the reversal behavior of a single microscopic unit cell. However, when we look into the reversal for the complete 25 unit cell geometry with boundaries, the reverse magnetization at the coercive field can be attributed to the nucleation of the reverse domain at the edges and the propagation of domain walls. Interestingly,

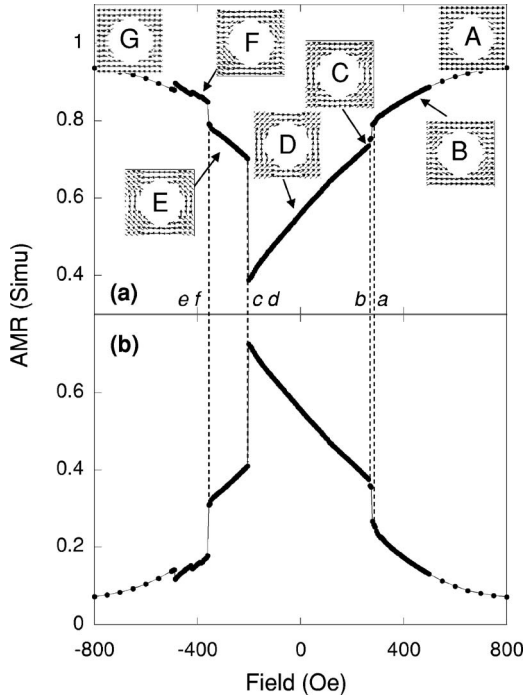


FIG. 8. Simulated LMR and TMR curves for $t=25$ nm, as the field sweeps from positive saturation to negative. Shown as insets in (a) are the spin states captured from OOMMF simulation at different field values.

domain-wall pinning during the wall propagation was not observed from the simulation, though it is usually expected from these structures.[7,8,10,12] To confirm the role of domain-wall pinning in the arrays, further *in situ* magnetic imaging techniques, such as Lorentz microscopy, are needed. Nevertheless, we can ascertain that the local spin rotation due to the various shape anisotropies introduced by the holes does play an important role in the hardening effect of the perforated film.

## CONCLUSION

We have investigated the magnetoresistance and magnetization reversal process in nanoscale $Ni_{80}Fe_{20}$ antidot arrays. We found that the current density is periodically modulated by the ordered antidot arrays, and the magnetization reversal process could be clearly identified from the shape of the MR traces. We also observed a marked increase in the coercive field as compared with the continuous film. For fixed antidot geometry, it was found that the magnetization reversal process is strongly dependent on the film thickness, which has been correlated with our magnetization hysteresis measurements. Our results are also in good agreement with the micromagnetic simulations.

## ACKNOWLEDGMENT

This work was supported by the National University of Singapore (NUS) under Grant No. R23-000-283-112. C.C.W. would like to thank NUS for financial support.

*Electronic address: eleaao@nus.edu.sg

[1] John B. Goodenough, Phys. Rev. **95**, 917 (1954).
[2] H. J. Williams and W. Shockley, Phys. Rev. **75**, 178 (1949).
[3] L. J. Dijkstra and C. Wert, Phys. Rev. **79**, 979 (1950).
[4] P. Gaunt, Philos. Mag. B **48**, 261 (1983).
[5] James A. Jatau and Edward Della Torre, J. Appl. Phys. **78**, 4621 (1995).
[6] Brandon Edwards and D. I. Paul, J. Magn. Magn. Mater. **147**, 331 (1995).
[7] R. P. Cowburn, A. O. Adeyeye, and J. A. C. Bland, Appl. Phys. Lett. **70**, 2309 (1997); J. Magn. Magn. Mater. **173**, 193 (1997).
[8] A. O. Adeyeye, J. A. C. Bland, and C. Daboo, Appl. Phys. Lett. **70**, 3164 (1997).
[9] Kai Liu and C. L. Chien, IEEE Trans. Magn. **34**, 1021 (1998).
[10] W. Y. Lee, H. T. Leung, W. Zhang, Y. B. Xu, A. Hirohata, C. C. Yao, B.-Ch. Choi, D. G. Hasko, and J. A. C. Bland, IEEE Trans. Magn. **35**, 3475 (1999).
[11] A. Yu. Toporov, R. M. Langford, and A. K. Petford-Long, Appl. Phys. Lett. **77**, 3063 (2000).
[12] U. Welp, V. K. Vlasko-Vlasov, G. W. Crabtree, Carol Thompson, V. Metlushko, and B. Ilic, Appl. Phys. Lett. **79**, 1315 (2001).
[13] P. Vavassori, G. Gubbiotti, G. Zangari, C. T. Yu, H. Yin, H. Jiang, and G. J. Mankey, J. Appl. Phys. **91**, 7992 (2002).
[14] Nicholas Owen, Hang-Yan Yuen, and Amanda Petford-Long, IEEE Trans. Magn. **38**, 2553 (2002).
[15] Z. L. Xiao, Catherine Y. Han, U. Welp, H. H. Wang, V. K. Vlasko-Vlasov, W. K. Kwok, D. J. Miller, J. M. Hiller, R. E. Cook, G. A. Willing, and G. W. Crabtree, Appl. Phys. Lett. **81**, 2869 (2002).
[16] I. Guedes, M. Grimsditch, V. Metlushko, P. Vavassori, R. Camley, B. Ilic, P. Neuzil, and R. Kumar, Phys. Rev. B **67**, 024428 (2003).
[17] L. J. Heyderman, F. Nolting, and C. Quitmann, Appl. Phys. Lett. **83**, 1797 (2003).
[18] C. C. Wang, A. O. Adeyeye, and Y. H. Wu, J. Appl. Phys. **94**, 6644 (2003).
[19] F. J. Castaño, K. Nielsch, C. A. Ross, J. W. A. Robinson, and R. Krishnan, Appl. Phys. Lett. **85**, 2872 (2004).
[20] C. C. Wang, A. O. Adeyeye, Y. H. Wu, and M. B. A. Jalil, J. Appl. Phys. **97**, 023521 (2005).
[21] C. T. Yu, H. Jiang, L. Shen, P. J. Flanders, and G. J. Mankey, J. Appl. Phys. **87**, 6322 (2000).
[22] A. Yu. Topoirov, Tech. Phys. **47**, 136 (2002).
[23] N. Singh, S. Goolaup, and A. O. Adeyeye, Nanotechnology **15**, 1539 (2004).
[24] Robert H. Norton, IEEE Trans. Magn. **MAG-19**, 1579 (1983).
[25] M. B. A. Jalil, S. L. A. Phoa, S. L. Tan, and A. O. Adeyeye, IEEE Trans. Magn. **38**, 2556 (2002).
[26] J. Guo and M. B. A. Jalil, J. Appl. Phys. **93**, 7450 (2003).
[27] S. Goolaup, N. Singh, A. O. Adeyeye, V. Ng, and M. B. A. Jalil, Eur. Phys. J. B **44**, 259 (2005).
[28] M. J. Donahue and D. G. Porter, http://math.nist.gov/oommf